Contents lists available at ScienceDirect

Arabian Journal of Chemistry

journal homepage: www.ksu.edu.sa

Original article

Green and sustainable synthesis of mesoporous silica from agricultural biowaste and functionalized with TiO_2 nanoparticles for highly photoactive performance

Tzong-Horng Liou [a,b,c,d,*], Rui-Ting Liu [a], Yu-Chen Liao [a], Chi-En Ku [a]

[a] Department of Chemical Engineering, Ming Chi University of Technology, 84 Gungjuan Rd., Taishan, New Taipei 24301, Taiwan
[b] Battery Research Center of Green Energy, Ming Chi University of Technology, 84 Gungjuan Rd., Taishan, New Taipei 24301, Taiwan
[c] R&D Center of Biochemical Engineering Technology, Ming Chi University of Technology, 84 Gungjuan Rd., Taishan, New Taipei 24301, Taiwan
[d] Department of Chemical and Materials Engineering, Chang Gung University, 259 Wenhua 1st Rd., Guishan Dist., Taoyuan City 33302, Taiwan

ARTICLE INFO

Keywords:
Rice husk
Mesoporous catalyst
Functionalization
Adsorption
Photocatalysis

ABSTRACT

Rice husk (RH) is a bio-based material and can be a valuable source of bioenergy. Burning RH to produce thermal energy results in the generation of RH ash (RHA). RHA contains abundant silica. This study prepared mesostructured RH–SBA-15 by using RHA as a silicon source. A nanosized TiO_2 photocatalyst was then synthesized using RH–SBA-15 as the support material. XRD and TEM confirmed that TiO_2 nanoparticles with mainly anatase structures were adequately dispersed in the hexagonal mesopores of the RH–SBA-15 sample. The TiO_2 particles had crystalline sizes of 6.5–7.9 nm and band gap energies of 3.45–3.47 eV. FTIR and XPS spectra verified that TiO_2 had been successfully combined with the SiO_2 material. The composite catalysts had surface areas of 248–383 m^2/g, pore volumes of 0.425–0.575 cm^3/g, and pore sizes of 6.12–6.35 nm. Calcination temperature, a parameter in the catalyst production process, strongly influenced the surface characteristics and pore structures of the composite catalysts. We also investigated the photodegradation of reaction blue 4 (RB4) with the composite catalysts. The catalyst's photoactivity was affected by adsorbent type, RB4 concentration, agitation speed, and calcination temperature. In addition, this study explored the photodegradation kinetics and mechanism. Converting RHA into SBA-15-based catalyst composites not only eliminates the disposal problem of agricultural waste, but also provides valuable information on wastewater purification.

1. Introduction

RH is an agricultural waste with high enthalpy (12,600 kJ/kg) (Krishnarao et al., 2001). This waste can be employed as a renewable and sustainable source of biomass energy and could thus help reduce greenhouse gas emissions (Prasara-A and Gheewala, 2017). The major components of RH are cellulose, hemicellulose, and lignin (Balasubramanian and Venkatachalam, 2023). However, a considerable quantity of RH ash (RHA) is produced during the thermal energy conversion of RH. The annual global output of RHA is approximately 160 million tons (Mosaberpanah and Umar, 2020). Dumping RHA in landfills is inappropriate because it can cause secondary pollution. RHA consists of 85–90 wt% amorphous silica. Conventional practices utilized RHA as a substitute for cement in building materials (Ma et al., 2023). RHA can also be employed in cleaner production of geopolymers and stabilization of soil (Raja et al., 2022; Hossain et al., 2021). In addition, a simple alkali extraction procedure can be used to recover silica in the form of high-quality mesoporous SBA-15 from RHA. SBA-15 has uniform mesopores and a large surface area and has thus received considerable great interest in terms of its potential in adsorption (Huang et al., 2023), catalysis (Liu et al., 2024), hydrogen storage (Wang and Bai, 2023), sensor (Ziarani et al., 2022), supercapacitor (Subramani et al., 2022), and drug delivery (Ulagesan et al., 2022) applications. Reactive blue 4 (RB4), an anionic compound, is widely used in the textile industry to dye materials such as nylon, silk, wool, viscose, and cotton. Incomplete removal of dyes from dye-treatment wastewater is likely to lead to the pollution of surface water and rivers (Teixeira et al., 2021). Conventional approaches to treating organic pollutants in water treatment plants—such as ion exchange, membrane filtration, and adsorption techniques—are insufficient for removing dyes. Photoassisted advanced

* Corresponding author at: Department of Chemical Engineering, Ming Chi University of Technology, 84 Gungjuan Rd., Taishan, New Taipei 24301, Taiwan.
E-mail address: thliou@mail.mcut.edu.tw (T.-H. Liou).

https://doi.org/10.1016/j.arabjc.2024.105764
Received 2 February 2024; Accepted 29 March 2024
Available online 30 March 2024

(a) (b)

Fig. 1. The optical photographs of (a) RH and (b) RH-SBA-15.

oxidative processes are the most widely used methods to eliminate organic contaminants (Sales et al., 2023).

Researchers have developed several types of photocatalysts for wastewater treatment, such as titanium dioxide, tungsten trioxide, silver bromide, and carbon nitride catalysts (Jo et al., 2023). Photocatalytic effects of environmental wastes and dyes used in industrial practices may have negative effects on living systems, especially on DNA (Arslan and Ili, 2015). TiO_2 photocatalyst is highly effective in the degradation of harmful gases, unpleasant odors, and wastewater because of its high stability, low cost, and nontoxicity. The material has broad applications, including in fuel cells (Tan et al., 2024) and for H_2 production (Yuan et al., 2024), CO_2 reduction (Urbanek et al., 2023), and wastewater purification (Rajendran et al., 2023). However, the photocatalytic activity of TiO_2 is limited because TiO_2 particles aggregate in water-based media, and this aggregation reduces the catalyst surface area. Furthermore, because of the small size of TiO_2 particles (20–30 nm), the rate of TiO_2 recovery is too low for practical applications. The aforementioned problems can be effectively solved by combining TiO_2 with a porous support material to improve the dispersion of catalyst sites, thereby promoting the material's efficiency and also reducing the cost of recovering the catalyst after the catalytic reaction. Numerous types of support materials can be employed to promote the photocatalytic efficiency of TiO_2. Asma and Hossein (2019) synthesized a TiO_2 photocatalyst immobilized within an FSM-16 mesoporous material (FSM = Folded Sheet Mesoporous). The surface area of TiO_2/FSM-16 photocatalyst (876.49 m^2/g) was much higher than TiO_2/MCM-41 photocatalyst (400.76 m^2/g). The composite catalyst was found to efficiently remove benzothiophene and dibenzothiophene. Chen et al (2020) prepared a carbon nanotube (CNT)–TiO_2 composite. The composite had a high specific surface area of 129.20 m^2/g and pore volumes of 0.292 cm^3/g. The nanotubes, with a conductive structure, improved electron–hole separation, resulting in a higher photolysis rate. Garcia et al (2021) investigated the addition of 7 % anatase TiO_2 to a SBA-15 mesoporous material. The catalyst composite had a high surface area of 732 m^2/g and average pore size of 6.0 nm. They found that SBA-15 possessed uniform cylindrical pores, which could effectively remove arsenic. Luo et al (2023) reported that Al fumarate and TiO_2 were loaded onto corrugated paper through a hierarchical self-assembly method; the loaded Al fumarate, which has a high surface area (1117.82 m^2/g) and high porosity (0.47 cm^3/g), acted as an excellent adsorbent, capturing organic dye molecules. Elmersly et al (2023) synthesized three-dimensional TiO_2–layered double-hydroxide composites for degrading the antibiotic sulfaguanidine. Because of its high surface area and tunable composition, the layered double hydroxide increased the catalytic activity, charge separation, and light adsorption of the TiO_2 catalyst. Compared with the characteristics of other materials, SBA-15 has a large specific area (500–800 m^2/g), highly ordered mesoporous channels, high thermal stability, and transparency to UV illumination, meaning that it can promote the photoactivity of a TiO_2 catalyst (Paulista et al., 2024). Thus, preparation of valuable TiO_2–SBA-15 nanocomposite byproducts by using RHA as a source of silicon is an appealing research topic.

Previous studies had already reported the preparation of titania-based catalyst composites. However, studies on SBA-15-based TiO_2 composites prepared from RHA for effective photodegradation of anionic dyes such as RB4 are less investigated. This lack in existing literature is a motivation for the present study. In the present study, RHA served as a renewable source of silicon in the production of SBA-15 supports. The mesopores of SBA-15 were then filled with TiO_2 nanoparticles through an incipient wetness impregnation method. The cost of raw catalysts can be reduced by fabricating SBA-15 using sodium silicate acquired from RHA waste through alkali extraction. In photocatalysis involving TiO_2, the calcination temperature is a crucial parameter affecting the particle size and crystal phase of TiO_2 particles as well as the degree of contaminant degradation that is achieved. We analyzed the structural features of the prepared composite material, including its pore volume, surface area, mesoporous and crystalline phases, band gap energy, surface morphology, and functional groups. Furthermore, we also investigated the heterogeneous photocatalytic degradation of RB4 dye. A UV–visible (UV–Vis) spectrophotometry was employed to evaluate the adsorption and photocatalytic ability of catalysts of multiple types and for various initial RB4 concentrations, agitation speeds, and calcination temperatures. Finally, we conducted a kinetic study to determine the rate constants for the photocatalytic reaction.

2. Materials and methods

2.1. Chemicals

RH was obtained from a rice mill in Taoyuan City, Taiwan. The fundamental composition and properties of the RH were reported in earlier papers (Liou and Yang, 2011; Liou and Wu, 2010). The optical photograph of RH is shown in Fig. 1a. The reagents employed in the preparation of catalyst samples were Pluronic triblock copolymer (P123, Sigma-Aldrich), titanium tetrachloride ($TiCl_4$, 99 vol%, Seedchem), RB 4 ($C_{23}H_{14}Cl_2N_6O_8S_2$, molecular weight = 637.43 g/mol, 35 wt%, Alfa Aesr), mixed gas (21 vol% O_2 and 79 vol% N_2, 99.995 %, Sun Fu Co.), and N_2 (99.995 %, Sun Fu Co.). Ethanol (99.9 vol%), sodium hydroxide,

sulfuric acid, and hydrochloric acid were purchased from Merck. All reagents used were of analytical grade.

2.2. Extraction of silicon from RH

First, the RH was rinsed with distilled water to withdraw soil and dust (Liou et al., 2022a). Next, the RH was immersed in hot hydrochloric acid solution to remove metal residue. The RH was then pyrolyzed in a quartz tube containing N_2 at 700 °C for 30 min, which yielded a silica–carbon composite. Through stirring and heating, sodium silicate solution was acquired by dissolving the silica in 1.5 M sodium hydroxide solution at 100 °C for 1 h. Finally, the silicate solution was subjected to filtration to remove carbon solids.

2.3. Fabrication of RH–SBA-15 support

SBA-15 material was fabricated from the RHA waste by following a hydrothermal treatment procedure (Liou et al., 2023; Zhang et al., 2023). First, 2.0 g of P123 was dissolved in 125 mL of 2.0 M HCl solution. Subsequently, 50 mL of sodium silicate solution (collected from RHA) was placed in the surfactant mixture, which was violently agitated at 35 °C for 15 min. Subsequently, the mixture was left without agitation for more than 24 h at 35 °C. The sample was then transferred to a Teflon cup, which was placed in a stainless steel autoclave and maintained at 100 °C for 24 h. After the hydrothermal process, a solid was collected through filtration, water-washing, and 24 h of drying at 60 °C. Finally, white powder (named RH–SBA-15) was obtained by calcining the solid sample under air at 550 °C for 6 h. The optical photograph of RH-SBA-15 is shown in Fig. 1b.

2.4. Preparation of pure TiO_2 and TiO_2/RH–SBA-15 photocatalyst

Samples of TiO_2-nanoparticle-functionalized RH–SBA-15 were synthesized using an incipient wetness impregnation method (Signoretto et al., 2010). Before being impregnated with $TiCl_4$, the RH-SBA-15 was preheated at 60 °C for 2 h to remove the adsorbed water. Then, a constant amount of $TiCl_4$ was slowly added to the RH-SBA-15 (1.5 g), with thorough mixing by ultrasonic vibration at room temperature for 10–15 min. The mixture was then dried at 60 °C for 24 h and calcined in air at 500–900 °C for 4 h. The filling ratio of TiO_2 nanoparticles was 7.439 %, which was calculated from the volume of TiO_2 nanoparticles divided by the pore volume of RH-SBA-15. The resulting specimen was denoted RH–TS. By comparison, pure TiO_2 catalyst was fabricated by employing the same heat-treatment procedure but without the addition of RH–SBA-15.

2.5. Photocatalysis test

The photocatalytic activity of RH–TS was tested, and TiO_2 and RH–SBA-15 samples were also tested for comparison (Liou et al., 2022b). The test involved the degradation of RB4 under irradiation with a 64-W UV lamp (Panchum/PR-1000, 365 nm). In a typical test, RB4 solution with an initial RB4 concentration of 20 mg/L was mixed with 200 mg of catalyst under stirring speed of 300 rpm. The solution's pH was regulated to 3.0 by using standard H_2SO_4 solution. Before light irradiation was initiated, the solution was allowed to reach equilibrium over 30 min. The photocatalytic tests were then conducted under UV irradiation for 120 min. Residual dye in the solution was collected through centrifugation and filtration by using a syringe filter over a constant period. The dye concentration was analyzed using a UV–Vis spectrophotometer (Thermo Genesys 10S) at an excitation wavelength of 599 nm. The photodegradation efficiency (X, %) of a catalyst was determined as follows:

$$X = \frac{C_o - C}{C_o} \times 100 \quad (1)$$

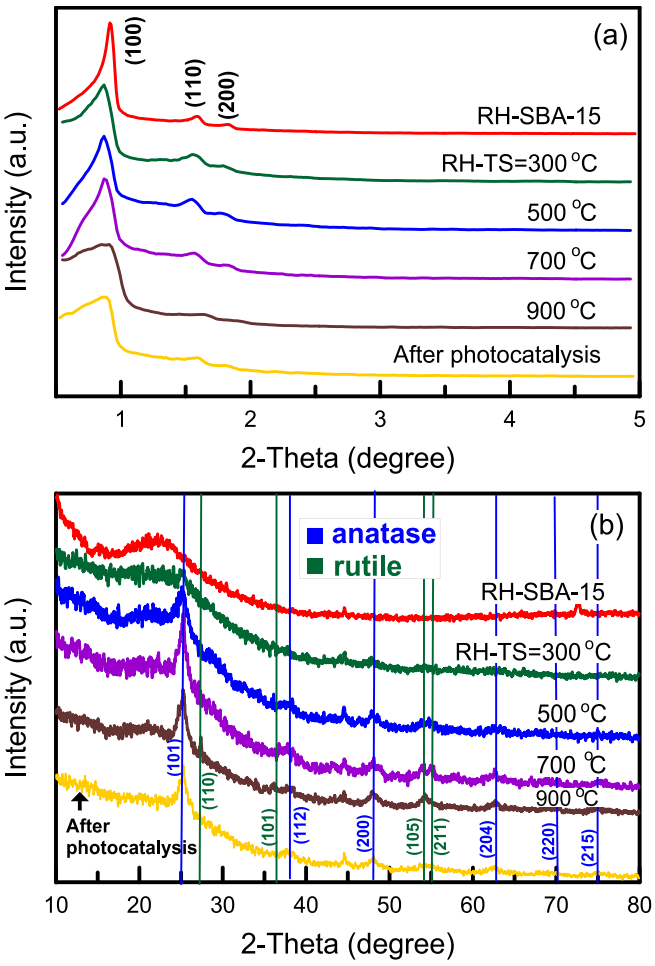

Fig. 2. (a) Low angle and (b) wide angle XRD patterns of catalyst specimens at various calcination temperatures.

where C_0 and C are the initial and instantaneous concentrations of RB4, respectively.

The catalysts were regenerated through a thermal treatment procedure. After being used for dye photodegradation, a dye–catalyst sample was rinsed with ethanol and deionized water and then heated to 500 °C for 2 h. The regeneration and photocatalytic tests were performed four times.

2.6. Characterization of materials

The pore volume and Brunauer–Emmett–Teller surface area of the composite samples were determined using a N_2 adsorption–desorption analyzer (Micrometric, ASAP 2020). The Barrett–Joyner–Halenda method was employed to obtain the pore size distribution from the desorption branch of the nitrogen sorption isotherm. The structures of the RH–SBA-15 matrix and TiO_2 nanocrystals were measured using Cu-kα radiation X-ray diffraction (XRD; PANalytical, model X'pert pro system) at low and high 2θ angles of 0.5°–5° and 10°–80°. Fourier transform infrared spectroscopy (FTIR; Shimadzu, model FTIR-8300) over the wavelengths 400 to 4000 cm^{-1} was performed to determine the functional groups on the composite catalysts. UV–Vis (model JASCO V-670) was employed to evaluate the optical properties of the catalyst samples.

The catalysts' morphological features were examined using field-emission scanning-electron microscopy (FE-SEM; JSM-6700F, JEOL) and transmission electron microscopy (TEM; JEM-1200CX II, JEOL). The particle size distributions of the RH–TS samples were determined

Table 1
Surface area, band gap energy, and crystallite size of catalyst samples.

Sample	S_{BET} (m^2/g)	V_t (cm^3/g)	V_{meso} (cm^3/g)	V_{mic} (cm^3/g)	V_{meso}/V_t (%)	d_P (nm)	D_P (nm)	eV	λ (nm)	Ti (wt%)
RH-SBA-15	501	0.889	0.884	0.005	99.4	6.56	–	–	–	–-
300 °C	383	0.554	0.541	0.013	97.7	6.20	6.5	3.45	359.4	36.29
500 °C	361	0.575	0.567	0.008	98.6	6.35	6.7	3.45	359.4	34.53
700 °C	325	0.538	0.533	0.005	99.1	6.12	7.5	3.47	357.3	34.24
900 °C	248	0.425	0.422	0.003	99.3	6.26	7.9	3.47	357.3	33.19

S_{BET} = specific surface area, V_t = total pore volume, V_{mic} = micropore volume, V_{meso} = mesopore volume, dp = pore diameter (BJH desorption), D_P = crystallite size, eV = band gap energy, λ = X-ray wavelength, Ti content is determined by ICP-MS.

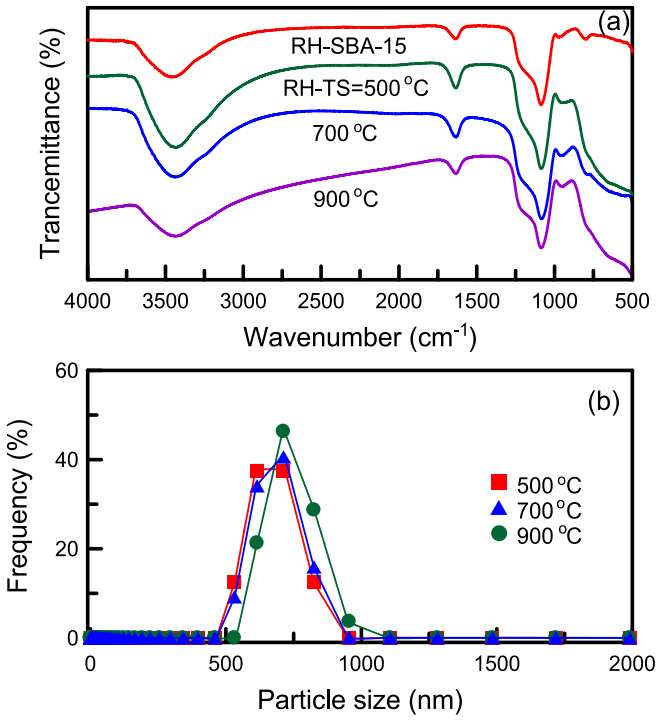

Fig. 3. (a) FTIR spectra and (b) particle size distribution of catalyst specimens at different calcination temperatures.

through dynamic light scattering (DLS), which was implemented using a Malvern Zetasizer Nano ZS90 spectrophotometer. The elemental composition of a photocatalyst's surface was examined through X-ray photoelectron spectroscopy (XPS; 250 Xi, Thermo Scientific Esca Lab). The Ti content in the catalyst composites was determined using an inductively coupled plasma-mass spectrometer (ICP-MS; S-35, Konton Plasmakon).

3. Results and discussion

3.1. Characterization of structure and composition

XRD patterns were obtained at wide angles (10°–80°) and low angles (0.5°–5°) to determine the pore structure and crystalline phase of the pure RH–SBA-15 and RH–TS samples. The pattern of the pure RH–SBA-15 sample (Fig. 2a) contained (100), (110), and (200) diffraction peaks, which were attributed to the SBA-15 structure with a two-dimensional hexagonal array and ordered mesopores (Liu et al., 2024). The patterns of the RH–TS samples synthesized at various calcination temperatures were similar to that of the RH–SBA-15 sample, indicating that the incipient wetness impregnation method did not destroy the mesostructure of SBA-15. For the RH–TS samples, increasing the calcination temperature resulted in the three diffraction peaks shifting to higher 2θ values; this was attributable to the TiO_2 particles being larger when the calcination temperature was higher (Sales et al., 2023). Fig. 2b shows a broad peak at 2θ = 15°–30° in the pattern of the pure RH–SBA-15 sample; this peak is characteristic of amorphous SiO_2 (Xu et al., 2023). The diffraction peaks in the patterns of all RH–TS samples were clearly related to the anatase and rutile phases of TiO_2 nanocrystals. The anatase phase was concluded to be the main TiO_2 structure in the samples. When the calcination temperature was increased from 300 to 900 °C, the intensity of the peaks corresponding to the anatase phase also increased. Yang et al (2006) observed the phase change of TiO_2 nanocrystals within the mesoporous silica matrix and concluded that the silica pores prevented the transformation of the nanocrystals from the anatase phase to the rutile phase. This observation suggests that TiO_2 remains relatively stable even at high temperatures. We evaluated the crystallite size D_p of TiO_2 in our RH–TS samples by using the Scherrer equation (Qamar et al., 2024):

$$D_p = \frac{0.89\lambda}{\beta cos(\theta)} \quad (2)$$

where θ is the diffraction angle at the peak maximum, β is the full width at half maximum of the most intense diffraction peak, and λ is the X-ray wavelength. As revealed in Table 1, the TiO_2 crystallite sizes were in the range of 6.5–7.9 nm and increased with the calcination temperature. The comparison of the XRD patterns before and after the photocatalysis reaction was also shown in Fig. 2a and 2b. After the photocatalysis reaction, the catalyst still exhibited three (100, 110, and 200) peaks as well as the anatase and rutile phases of TiO_2 structure. The observation indicated that the mesophase and crystal structure of photocatalyst were not destroyed.

The FTIR spectra of the composite catalysts are presented in Fig. 3a. In the spectra of the pure RH–SBA-15 and RH–TS samples, the peaks at 980 and 1635 cm^{-1} were attributable to the existence of silanol OH groups (Chaabane et al., 2023). The broad peak at approximately 3400 cm^{-1} was ascribed to stretching of hydroxyl groups (OH) in water. The bands at 1090, 790, and 450 cm^{-1} corresponded to the stretching and bending vibrations of Si–O–Si groups, respectively (Chen and Huang, 2023). The peak at 910–960 cm^{-1} was attributable to Si–O–Ti groups (Acosta-Silva et al., 2011). The interaction of TiO_2 with SiO_2 on the walls of the RH–SBA-15 mesopores resulted in the formation of TiO_2–SiO_2 composites. The intensity of the peak at 910–960 cm^{-1} was increased when the calcination temperature was raised. The weak peak at 570 cm^{-1} corresponded to a Ti–O–Ti structure (Parnicka et al., 2022). However, the peak could not be clearly observed in the spectra, suggesting that the TiO_2 amount might need to be increased. Fig. 3b displays the particle size distributions of the mesoporous RH–TS materials obtained at various calcination temperatures. These distributions were measured through DLS. Additionally, the Brownian motion of the RH–TS particles was observed to enable the analysis of their size (Kim et al., 2013). The mean sizes of RH–TS particles prepared at calcination temperatures of 500, 700, and 900 °C were 667.5, 680.3, and 732.8 nm, respectively; thus, increasing the calcination temperature led to an increase in particle size.

The UV–Vis absorption spectra of the pure RH–SBA-15 sample and the RH–TS samples obtained at various calcination temperatures are

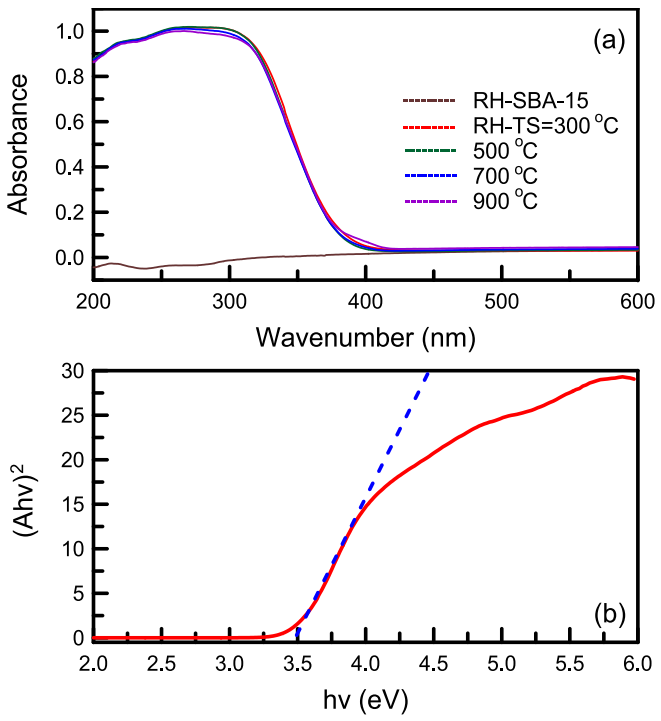

Fig. 4. (a) UV–vis absorption spectra of catalyst specimens at different calcination temperatures, and (b) Band gap energy of RH-TS catalyst.

presented in Fig. 4a. The spectrum of the pure RH–SBA-15 sample contained no absorption peaks within the entire wavelength range. However, the spectra of the RH–TS samples had a wide absorption peak at 200–400 nm. The position of this peak shifted to lower wavelengths as the calcination temperature was increased. To confirm the validity of this observation, the E_{gap} values of the RH–TS samples were determined using the Kubelka–Munk method (Abdi et al., 2023):

$$(\alpha h\upsilon)^2 = A(h\upsilon - E_g) \tag{3}$$

where A, υ, h, and α are a constant, the light frequency, Planck's constant, and the absorption coefficient, respectively. E_{gap} values could be obtained by extrapolating the linear part of the plot in Fig. 4b. The E_{gap} values and wavelengths of the RH–TS catalysts were in the ranges of 3.45–3.47 eV and 357.3–359.4 nm, respectively (Table 1). Thus, the catalysts adsorbed photons with the wavelength of UV light.

XPS spectra were obtained to identify the elements on the surfaces of the catalyst samples. Fig. 5a presents the survey spectra of the RH–TS sample. The peaks in these spectra confirmed the existence of Si, Ti, O, and C (Wei et al., 2023). The weak carbon peak may have been due to residual carbon after the pyrolysis of RH. Fig. 5b shows the Ti 2p XPS spectrum of the RH–TS sample; this spectrum contained two peaks at 463.1 and 457.3 eV, which were associated with Ti $2p_{1/2}$ and Ti $2p_{3/2}$, respectively. This observation verifies that Ti^{4+} was the main form in which Ti existed (Liu et al., 2023a). Fig. 5c and 5e presents the Si 2p XPS spectra of RH–TS and RH-SBA-15 samples. RH-SBA-15 contained only one peak at 102.0 eV, which corresponded to the Si–O–Si bond. RH–TS sample contained two peaks at 102.5 and 101.9 eV, respectively, which could be attributed to the existence of Si–O–Ti and Si–O–Si bonds. The O 1 s XPS spectra of RH–TS and RH-SBA-15 samples were displayed in Fig. 5d and 5f. RH-SBA-15 contained two peaks at 531.9 and 531.0 eV, which corresponded to the Si-O–H and Si–O–Si bonds. RH–TS sample contained peaks at 533.2, 532.5, 531.7, and 528.7 eV, which corresponded to the functional groups of Si-O–H, Si–O–Si, Si-O-Ti, and Ti–O–Ti bonds, respectively (Cani et al., 2021). The observation indicated the combination of TiO_2 with SiO_2 on the surface of RH–SBA-15 walls. The Si-O-Ti groups could affect the surface activity of TiO_2 and

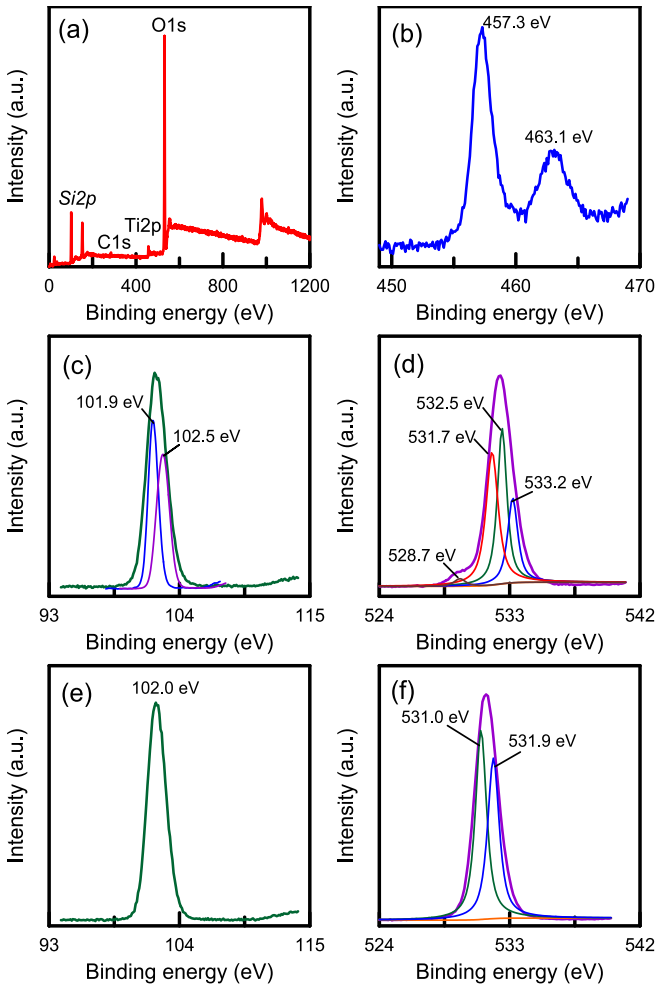

Fig. 5. XPS spectra of RH-TS catalyst (calcination temperature of 500 °C): (a) wide survey spectrum, (b) Ti 2p, (c) Si 2p, and (d) O 1 s. Pure RH-SBA-15: (e) Si 2p, and (f) O 1 s.

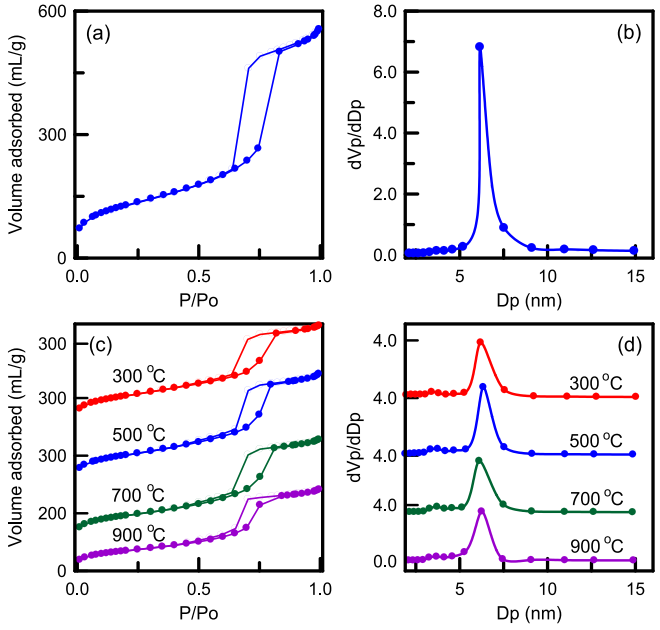

Fig. 6. N_2 sorption isotherm and pore size distribution of (a),(b) pure RH-SBA-15, and (c),(d) RH-TS catalysts at different calcination temperatures.

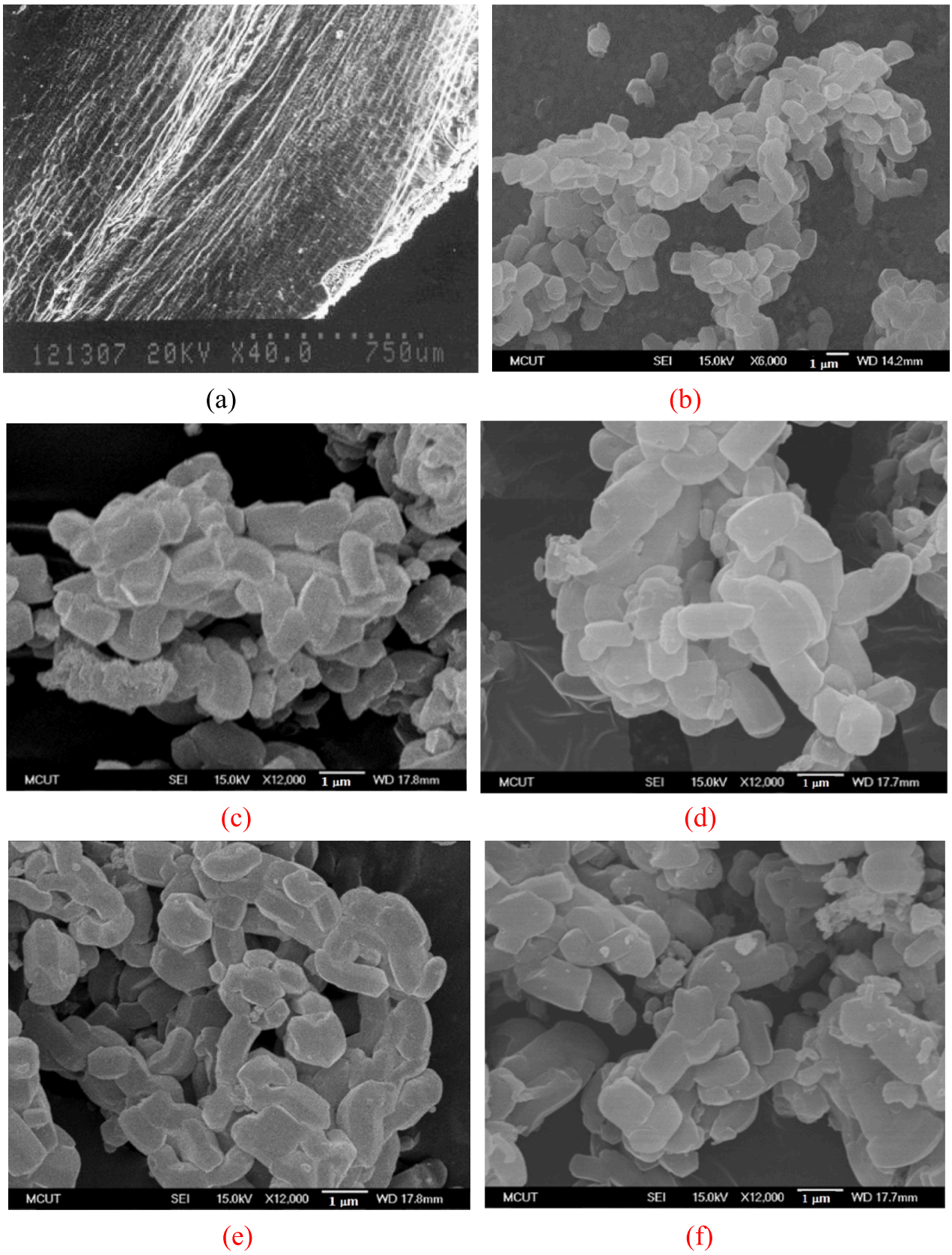

Fig. 7. FE-SEM images of (a) inner surface of RH, (b) pure RH-SBA-15, and RH-TS catalysts at calcination temperature of (c) 300 °C, (d) 500 °C, (e) 700 °C, and (f) 900 °C.

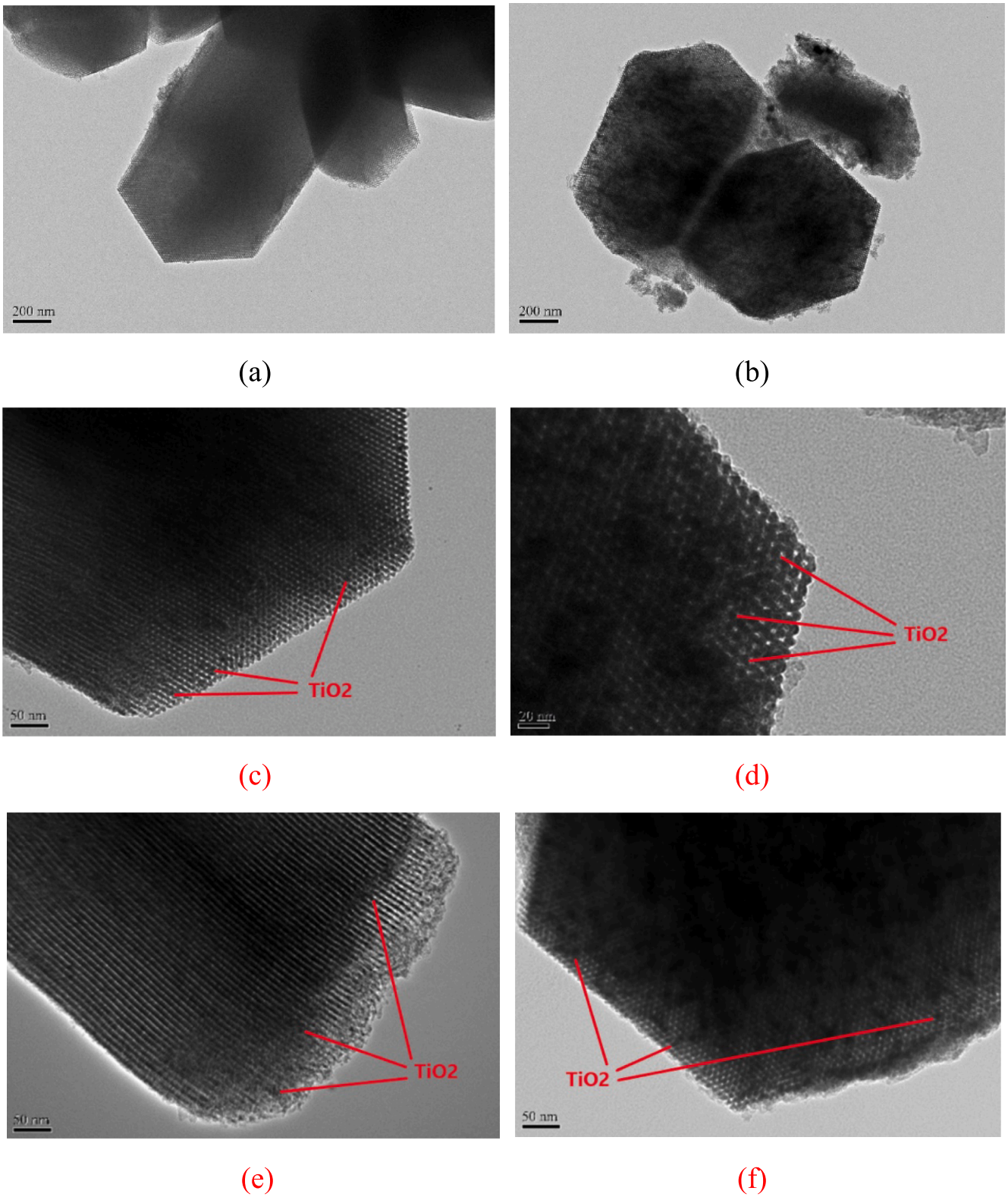

Fig. 8. TEM images of (a) pure RH-SBA-15, and RH-TS catalysts at calcination temperature of (b) 300 °C, (c) 300 °C, (d) 500 °C, (e) 700 °C, and (f) 900 °C.

thereby effectively increase the photocatalytic activity of the RH–TS catalysts.

3.2. *Textural features*

The nitrogen sorption isotherms of the pure RH–SBA-15 sample and the RH–TS samples obtained at various calcination temperatures (300–900 °C) are illustrated in Fig. 6a and 6c, respectively. All samples had type IV isotherms with H1 hysteresis loops, as determined in accordance with the categorization of the International Union of Pure and Applied Chemistry (IUPAC). The materials were thus typical mesoporous structures with cylindrical pores (Liu et al., 2023b). The

incorporation of TiO_2 nanoparticles did not change the pore framework of the RH–SBA-15 sample. The adsorbed volume observed for the RH–TS samples was the same for all calcination temperatures from 300 to 700 °C. However, increasing this temperature from 700 to 900 °C resulted in a clearly smaller adsorbed volume. TiO_2 agglomerations blocked the silica pores, resulting in a smaller adsorbed volume.

The pore size distribution of the pure RH–SBA-15 sample and composite catalysts obtained at different calcination temperatures are presented in Fig. 6b and 6d, respectively. The pure RH–SBA-15 sample had a narrow pore size distribution. This behavior indicated that the pore diameter of mesoporous silica was very uniform (average = 6.56 nm). The addition of TiO_2 nanoparticles to the RH–SBA-15 matrix reduced the average pore diameter to 6.20–6.35 nm. The slight reduction in the sizes of the catalyst's pores was probably due to small amounts of TiO_2 blocking the pore channels of the RH–SBA-15 sample. Furthermore, one small peak could be observed at approximately 3.5 nm, indicating the bimodal pore structure of the RH–TS materials. These small pores may have been holes formed by the agglomeration of TiO_2 nanoparticles within the RH–SBA-15 mesopores during the thermal treatment. The surface area and pore analysis of RH-SBA-15 and the catalyst samples are exhibited in Table 1. The surface area of pure RH-SBA-15 was 501 m^2/g and total pore volume was 0.889 cm^3/g. The surface area and pore volume of pure RH-SBA-15 were higher than those of RH-TS samples (248–383 m^2/g and 0.425–0.575 cm^3/g). The incorporation of TiO_2 particles into the pores of RH-SBA-15 led to a reduction in surface area and pore volume. The surface area and pore volume of RH-TS catalysts decreased if the calcination was increased. The surface area decreased greatly when the calcination temperature was increased to 900 °C, which was attributable to the existence of large TiO_2 particles in the mesoporous silica framework. The blockage of pore opening may have reduced the catalyst surface area. The pure RH-SBA-15 had the high mesoporosity of 99.4 %. The mesopore fractions of the RH-TS catalysts increased from 97.7 % to 99.3 % when the calcination temperature was increased from 300 to 900 °C. This observation indicates that the RH–TS samples were mainly composed of mesostructure. Additionally, RB4 is a medium-sized molecule. Our RH–SBA-15 substrate had relatively large pores, which could have allowed the rapid passage of RB4 dyes for adsorption and reaction with the TiO_2 catalyst. This phenomenon would have given the composite higher photocatalytic activity than that of the bare TiO_2 catalyst.

3.3. FE-SEM and TEM observations

FE-SEM analyses were conducted to understand the morphological change in the RH–SBA-15 material after it was modified. Fig. 7a reveals that inner surface of RH was rough. The pure RH–SBA-15 sample had irregular sharp cylinder-like particles, as depicted in Fig. 7b. A similar appearance was also observed in a previous study (Cavalcanti et al., 2023). The particles had an aggregated and homogeneous form. Fig. 7c-7f confirm that the shape of the RH–TS particles obtained at a calcination temperature of 300–900 °C was also cylinder-like. The catalyst samples were thus highly stable and not destroyed under the highest calcination temperature.

TEM was employed to inspect the distribution of TiO_2 particles within the mesoporous silica framework. The appearances of the pure RH–SBA-15 sample and the RH–TS samples are presented in Fig. 8a and 8b, respectively; these samples had a large-scale hexagonal structure comprising highly ordered mesopores (Khan et al., 2024). A self-assembly reaction between Na_2SiO_3 compounds and P123 micelles was responsible for this highly ordered skeleton. High-magnification TEM images of the RH–TS samples obtained at calcination temperatures of 300–900 °C are depicted in Fig. 8c–8f. Numerous small dark points (as marked with red arrows) were observed to be dispersed uniformly within the pores of the RH–SBA-15 sample; these points were TiO_2 nanoparticles with an average size of approximately 6.2–7.6 nm. The size of the TiO_2 particles was discovered to increase with the

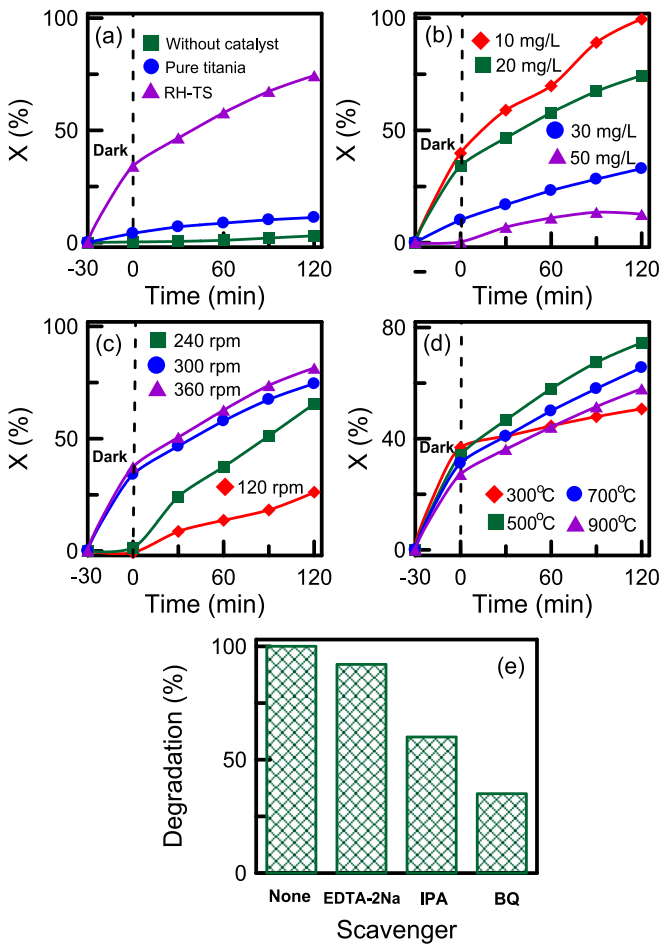

Fig. 9. Effect of reaction conditions on the photocatalytic activity of RH-TS catalysts: (a) various types of catalysts, (b) initial RB4 concentration, (c) agitation speed, (d) calcination temperature, and (e) photocatalytic tests in the presence of radical scavengers.

calcination temperature, and this finding was in good agreement with XRD results (Fig. 2b). The RH–SBA-15 material had a uniform pore distribution (Fig. 8c–8f). Moreover, in the images, no small dark points could be seen outside the RH–SBA-15 framework, indicating that the TiO_2 particles were well grown inside the RH–SBA-15 matrix. The highly dispersed TiO_2 nanocrystals did not destroy the mesostructure of the RH–SBA-15 material. These results are consistent with the observations for $TiO_2/SO_4/Ni$@SBA-15 catalysts reported by Yoganandhan et al (2023). Table 1 lists the weight percentages of Ti in the RH–TS samples. For all samples, the weight percentage of Ti decreased slightly with an increase in calcination temperature. A trace amount of the titanium precursor may have been evaporated at high calcination temperatures, resulting in the loss of TiO_2 during synthesis of the composite catalysts.

3.4. Photoactivity of RH–TS catalysts

Fig. 9a plots the rate of degradation of RB4 in the presence or absence of pure TiO_2 and the RH–TS catalysts. To determine whether RB4 was sensitive to UV light, we attempted to degrade the dye without a catalyst present; the degree of conversion was 3.1 % with 120 min of UV exposure. The degree of conversion did not change considerably, confirming that RB4 was stable during photolysis. A degree of conversion of 11.2 % was achieved when UV irradiation was performed in the presence of only pure TiO_2. This poor degradation could be ascribed to the aggregation of TiO_2 nanoparticles in the dye solution. The absence of active sites in the TiO_2 skeleton and the nanoparticles' blockage of the passage

of light caused the catalyst to have low photoactivity. The use of RH–TS resulted in the highest RB4 photodegradation; this was due to the TiO_2 nanoparticles being highly dispersed in the mesoporous silica material. The hybrid catalyst's high surface area meant that numerous active sites were available for RB4 degradation. In addition, during the photolysis experiment, the use of the RH–TS composite was found to result in two-stage dye degradation (Sharma and Kumari, 2008). After a period of 30 min in darkness, the reduction in RB4 concentration suggested the achievement of adsorption–desorption equilibrium. Upon subsequent UV exposure, the RB4 concentration decreased considerably, indicating that photocatalysis caused decomposition of RB4, with the degree of conversion increasing over time.

The influences of the initial RB4 concentration (10–50 mg/L) on the adsorption and photocatalytic efficiency of the RH–TS catalyst are illustrated in Fig. 9b. Lower RB4 concentrations resulted in higher removal efficiency levels. At a low RB4 concentration, the number of active sites available for adsorption was much higher than the number of dye molecules, resulting in photocatalytic efficiency being promoted. The removal efficiency of the catalyst was as high as 100 % after 120 min when the initial RB4 concentration was 10 mg/L. This observation confirms that RH–TS can effectively remove trace contaminants from wastewater solutions.

The speed at which a wastewater–catalyst mixture is agitated can affect the dispersion of dye in the mixture, which plays a critical role during photocatalysis. The influence of agitation speed on the adsorption and photocatalytic efficiency of the RH–TS catalysts is illustrated in Fig. 9c. The removal efficiency was higher when the agitation speed was higher. Increasing the agitation speed enhanced mass transfer between the dye and the catalyst and consequently increased the photolysis rate. The removal efficiency did not change considerably when the agitation speed was changed from 300 to 360 rpm. This signifies that the solute was uniformly dispersed in the solution. Film resistance can be neglected at high agitation speeds.

The effect of calcination temperature on the photodegradation activity of the RH–TS catalysts is displayed in Fig. 9d. Regarding the dark period lasting 30 min, the adsorption capacity of the catalyst was lower when a higher calcination temperature was used to produce the catalyst; this was due to the catalyst surface area being higher when the calcination temperature was lower (Table 1). The same trend was also observed at Fig. 6c that adsorbed volumes of catalysts increased with decreasing the calcination temperature. The higher surface area and adsorbed volume meant a higher number of adsorption sites and thus higher adsorption capacity. The highest removal efficiency was achieved by the catalyst obtained at a calcination temperature of 500 °C. This indicates that both the TiO_2 particle size and crystalline structure affected photocatalytic activity. Yang et al (2006) observed that the mesostructure of SBA-15 was beneficial to the thermal stability of anatase TiO_2 up to 800 °C. However, when the calcination temperature was higher, the TiO_2 particles were larger, leading to lower photoactivity. Although the proportion of the anatase phase was slightly low when the calcination temperature was 500 °C, the TiO_2 particle size had a stronger effect on catalytic activity than did the crystal structure. Additionally, the photoactivity of the catalyst obtained at a calcination temperature of 300 °C was the lowest, which was due to the absence of crystalline phases (anatase and rutile) in the TiO_2 structure, as shown in Fig. 2b.

The photocatalytic mechanism is studied by using scavengers. Scavengers selected disodium ethylene diamine tetraacetate (EDTA-2Na) to trap the hole (h^+), 1,4-benzoquinone (BQ) to trap the superoxide radical ($\cdot O_2^-$), and isopropanol alcohol (IPA) to trap the hydroxyl radical ($\cdot OH$), respectively (Srinithi et al., 2023). It was observed in Fig. 9e, the photocatalytic efficiency was dramatic decreased with the addition of BQ and IPA scavengers, indicating that both $\cdot O_2^-$ and $\cdot OH$ radicals were primarily responsible for the degradation of RB4 dye. However, photocatalytic efficiency was slightly decreased by using EDTA-2Na scavenger, indicating that h^+ was not the dominant active species during the photodegradation process. The mechanism underlying dye degradation in the presence of a porous composite photocatalyst is complex and can be divided into several steps, including bulk mass transfer, pore diffusion, surface adsorption, photocatalytic decomposition, and desorption. As shown in Fig. 10, the RH–SBA-15 sample, with a large surface area and high mesoporosity, provided numerous empty sites for the capture of RB4 adsorbate. Furthermore, electron–hole pairs were formed in the anatase TiO_2 nanoparticles when they absorbed UV light (Qin et al., 2023). The electrons reacted with O_2 to generate $\cdot O_2^-$. The holes interacted with H_2O or –OH groups to produce $\cdot OH$ (Cen et al., 2023). RB4 near the TiO_2 particles was decomposed by $\cdot O_2^-$ and $\cdot OH$ through photooxidation. The final products were H_2O, CO_2, and other degraded products (Sultana et al., 2023). The RH–SBA-15 support with large mesopores played a critical role in the adsorption–desorption reaction of dye molecules and decomposed products. Furthermore, the mesoporous framework of RH–SBA-15 limited the growth of TiO_2 crystalline structure and particle size. The photocatalytic activity of the catalyst was effectively promoted by the small size of the anatase TiO_2 particles. Accordingly, RH–TS composites are suitable for use as excellent adsorbents with high photoactivity for the removal of hazardous pollutants from wastewater solutions.

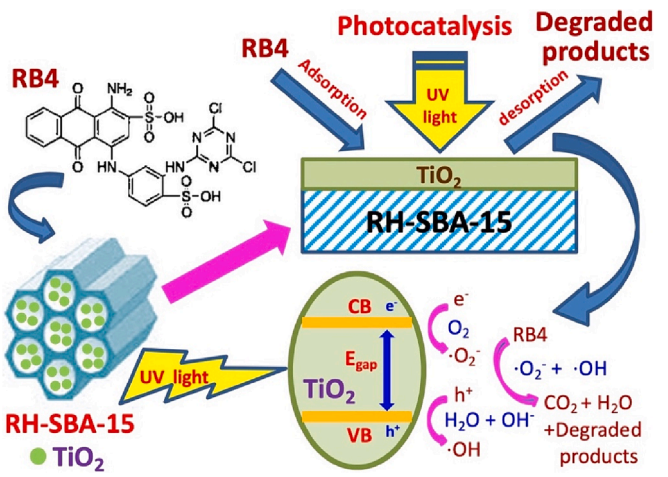

Fig. 10. Schematic diagram of adsorption and photocatalytic mechanism of RH-TS composites in the RB4 dye solution.

3.5. Evaluation of photodegradation rate

During the photocatalytic oxidation of organic matter, oxygen is usually abundant; thus, its concentration can be regarded as a constant. Therefore, the photocatalytic reaction can be assumed to be a quasi-first-order reaction (Bibi et al., 2023). The photocatalytic rate can be deduced from the Langmuir–Hinshelwood model (Kumar et al., 2023):

$$R = -\frac{dC}{dt} = \frac{k_r k_a C}{1 + k_a C} \tag{4}$$

where k_r and k_a are the reaction rate constant and adsorption coefficient, respectively. For low RB4 concentrations (denoted C), Eq. (4) can be rewritten as follows:

$$-\frac{dC}{dt} = k_r k_a C \tag{5}$$

By integrating Eq. (5) from time 0 to t, we acquire

$$\ln\left(\frac{C_o}{C_t}\right) = k_r k_a t \approx k_{app} t \tag{6}$$

where k_{app} is the apparent rate constant, C_t is the RB4 concentration at time t during photolysis, and C_0 is the RB4 concentration before light

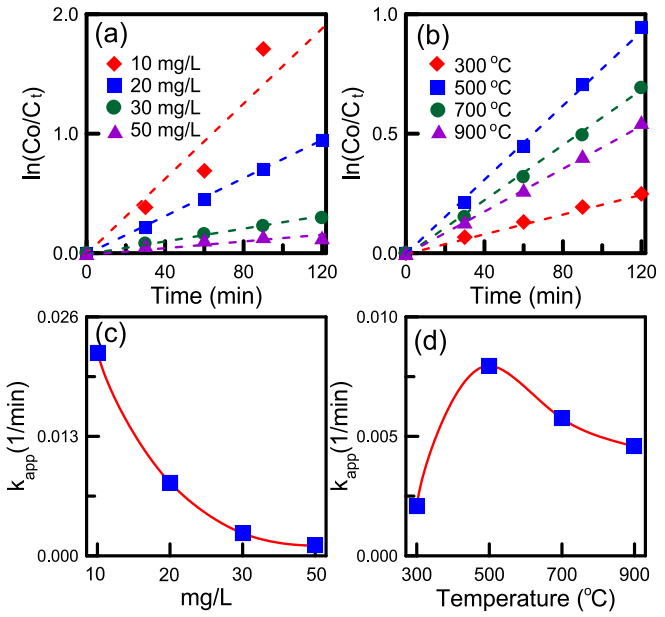

Fig. 11. The $\ln(C_o/C_t)$ versus time plots and apparent reaction rate constants for RB4 degradation: (a), (c) initial RB4 concentration, and (b),(d) calcination temperature.

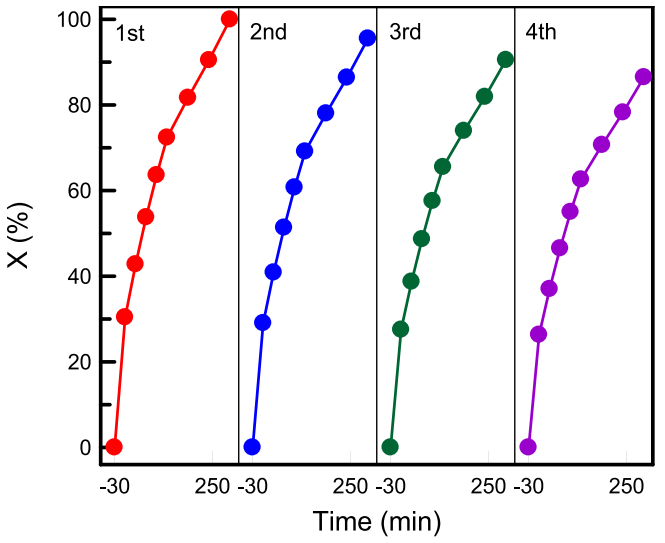

Fig. 12. Reutilization of RH-TS for RB4 photocatalysis experiments in four cycles.

irradiation.

The degradation kinetics of RB4 for various reaction conditions are illustrated in Fig. 11a and 11b. We estimated k_{app} through the least-squares method from the slope represented by Eq. (6). According to Fig. 11c, when the initial concentration was increased from 10 to 50 mg/L, the photocatalytic rate decreased. A calcination temperature of 500 °C resulted in the highest photocatalytic rate (Fig. 11d). These observations suggest that reducing the RB4 concentration increased the dispersion of the dye in the aqueous solution. A calcination temperature of 500 °C led to the formation of smallest TiO_2 nanocrystals with the more stable anatase structure. RH–SBA-15 had a high surface area and thus more active sites available for the elimination of RB4.

3.6. Reutilization experiments

The reusability of the RH–TS composites is crucial because catalyst regeneration reduces the cost of wastewater purification. As shown in Fig. 12, the photodegradation efficiency was still 86.21 % after the fourth run. This observation indicates the excellent reusability and high stability of the RH–TS nanocatalysts obtained using RHA as a sustainable silicon source.

4. Conclusion

In this study, SBA-15-based TiO_2 catalysts were prepared, with sustainable RHA serving as a silicon source for the fabrication of the support. The RH–SBA-15 had high adsorptive volumes and ordered mesopores that products and reactants can diffuse quickly through it. The incorporation of TiO_2 did not affect the mesoporous structure of the RH–SBA-15 material. The main TiO_2 phase was the anatase phase. The existence of Ti–O–Si bonds on the pore walls of the support can effectively increase the RH-TS photocatalytic activity. The isotherms of the RH–TS composites were type IV with an H1 hysteresis loop, indicating a mesoporous material with bimodal pore structure. Both adsorption and photolysis enhanced the catalyst's degradation efficiency. The removal efficiency of RB 4 on the RH–TS catalysts could be enhanced by reducing the initial RB4 concentration and increasing the agitation speed. Furthermore, the calcination temperature of 500 °C showed the highest photocatalytic activity. The results of this study were useful for simultaneously solving the problems of wastewater purification and agricultural waste recycling.

CRediT authorship contribution statement

Tzong-Horng Liou: Investigation, Methodology, Writing – original draft. **Rui-Ting Liu:** Supervision, Writing – review & editing. **Yu-Chen Liao:** Formal analysis, Validation. **Chi-En Ku:** Supervision, Data curation, Resources.

Declaration of competing interest

The authors declare that they have no known competing financial interests or personal relationships that could have appeared to influence the work reported in this paper.

Acknowledgments

The authors expressed thanks to the National Science and Technology Council (NSTC) of Taiwan for its financial supports under Project No. NSTC 112-2221-E-131-004.

References

Abdi, Z., Bagheri, O., Kazemzadehhojaghan, M., Khachatourian, A.M., 2023. In situ synthesis of polypyrrole/Nd-doped ZnO nanocomposite with enhanced visible light photocatalytic performance for the degradation of organic dyes. Mater. Chem. Phys. 296, 127248 https://doi.org/10.1016/j.matchemphys.2022.127248.

Acosta-Silva, Y.J., Nava, R., Hernández-Morales, V., Macías-Sánchez, S.A., Gómez-Herrera, M.L., Pawelec, B., 2011. Methylene blue photodegradation over titania-decorated SBA-15. Appl. Catal. B-Environ. 110, 108–117. https://doi.org/10.1016/j.apcatb.2011.08.032.

Arslan, I., Ili, P., 2015. Genotoxicological assessment of nebuloside-A a triterpenoid saponin compound on whole blood DNA. Int. J. Food Prop. 18 (11), 2374–2379. https://doi.org/10.1080/10942912.2014.971185.

Asma, H., Hossein, F., 2019. Application of FSM-16 impregnated by TiO2 as an efficient photocatalyst for elimination of benzothiophene and dibenzothiophene, adsorptive removal of degradation products by MCM-41. J. Ind. Eng. Chem. 76, 122–132. https://doi.org/10.1016/j.jiec.2019.02.026.

Balasubramanian, S., Venkatachalam, P., 2023. Valorization of rice husk agricultural waste through lignin extraction using acidic deep eutectic solvent. Biomass Bioenerg. 173, 106776 https://doi.org/10.1016/j.biombioe.2023.106776.

Bibi, S., Shah, S.S., Muhammad, F., Siddiq, M., Kiran, L., Aldossari, S.A., Mushab, M.S.S., Sarwar, S., 2023. Cu-doped mesoporous TiO2 photocatalyst for efficient degradation

of organic dye via visible light photocatalysis. Chemosphere 339, 139583. https://doi.org/10.1016/j.chemosphere.2023.139583.
Cani, D., van der Waal, J.C., Pescarmona, P.P., 2021. Highly-accessible, doped TiO2 nanoparticles embedded at the surface of SiO2 as photocatalysts for the degradation of pollutants under visible and UV radiation. Appl. Catal. A-Gen. 621, 118179 https://doi.org/10.1016/j.apcata.2021.118179.
Cavalcanti, W.E.C., Lopes, A.M.S., Pergher, S.B.C., Braga, T.P., 2023. Glycerol conversion in the presence of ethanol over CoFe2O4/SBA-15 mesoporous catalyst: Effect of the co-reagent on the catalytic performance. Microporous Mesoporous Mat. 361, 112743 https://doi.org/10.1016/j.micromeso.2023.112743.
Cen, L., Tang, T., Yu, F., Wu, H., Li, C., Zhu, H., Guo, Y., 2023. Fabrication of ZIF-8/TiO2 electrospinning nanofibers for synergistic photodegradation in dyeing wastewater. J. Ind. Eng. Chem. 126, 537–545. https://doi.org/10.1016/j.jiec.2023.06.042.
Chaabane, L., Nikolantonaki, M., Weber, G., Bezverkhyy, I., Chassagnon, R., Assifaoui, A., Bouyer, F., 2023. Functionalization of SBA-15 mesoporous silica for highly efficient adsorption of glutathione: Characterization and modeling studies. J. Taiwan Ins. Chem. Eng. 152, 105169 https://doi.org/10.1016/j.jtice.2023.105169.
Chen, Y., Huang, Y., 2023. Influence of ceria existence form on deactivation behavior of Cu-Ce/SBA-15 catalysts for methanol steam reforming. Int. J. Hydrog. Energy 48 (4), 1323–1336. https://doi.org/10.1016/j.ijhydene.2022.10.046.
Chen, Y., Qian, J., Wang, N., Xing, J., Liu, L., 2020. In-situ synthesis of CNT/TiO2 heterojunction nanocomposite and its efficient photocatalytic degradation of Rhodamine B dye. Inorg. Chem. Commun. 119, 108. https://doi.org/10.1016/j.inoche.2020.108071.
Elmersly, L., Elmouchtari, E., Belghiti, M., Belkodia, K., Edaala, M.A., Briche, S., Tahiri, A.A., Rafqah, S., 2023. Development of a new composite LDH/TiO2-3D for degradation of sulfaguanidine under UV and visible light: Experimental design, kinetic and mechanisms. J. Environ. Chem. Eng. 11, 111038 https://doi.org/10.1016/j.jece.2023.111038.
Hossain, S.S., Roy, P.K., Bae, C.J., 2021. Utilization of waste rice husk ash for sustainable geopolymer: A review. Constr. Build. Mater. 310, 125218 https://doi.org/10.1016/j.conbuildmat.2021.125218.
Huang, G., Mao, D., Zhang, Y., Chen, X.D., Wu, Z., 2023. Postsynthesis of β-FeOOH/SBA-15 composites via mild ozone treatment: Effective surfactant removal and perfect property preservation for enhanced arsenic adsorption. J. Environ. Chem. Eng. 11, 109597 https://doi.org/10.1016/j.jece.2023.109597.
Jo, S., Im, S., Weon, S., Shin, H., Lim, J., 2023. Reduced TiO2 nanotube arrays as environmental catalysts that enable ad- vanced oxidation processes: A mini review. Chem. Eng. J. 477, 147031 https://doi.org/10.1016/j.cej.2023.147031.
Khan, H.A., Abou-Daher, M., de Freitas, A.L.S., Subburaj, J., Tall, O.E., Farooq, A., 2024. Performance studies of Pt, Pd and PtPd supported on SBA-15 for wet CO and hydrocarbon oxidation. Catal. Today 426, 114370. https://doi.org/10.1016/j.cattod.2023.114370.
Kim, H.J., Jeon, J.D., Kwak, S.Y., 2013. Highly dispersed mesoporous TiO2 spheres via acid treatment and its application for dye-sensitized solar cells. Powder Technol. 243, 130–138. https://doi.org/10.1016/j.powtec.2013.02.036.
Krishnarao, R.V., Subrahmanyam, J., Kumar, T.J., 2001. Studies on the formation of black particles in rice husk silica ash. J. Eur. Ceram. Soc. 21, 99–104. https://doi.org/10.1016/S0955-2219(00)00170-9.
Kumar, A., Raorane, C.J., Syed, A., Bahkali, A.H., Elgorban, A.M., Raj, V., Kim, S.C., 2023. Synthesis of TiO2, TiO2/PAni, TiO2/PAni/GO nanocomposites and photodegradation of anionic dyes Rose Bengal and thymol blue in visible light. Environ. Res. 216, 114741 https://doi.org/10.1016/j.envres.2022.114741.
Liou, T.H., Liu, S.M., Chen, G.W., 2022a. Utilization of e-wastes as a sustainable silica source in synthesis of ordered mesostructured titania nanocomposites with high adsorption and photoactivity. J. Environ. Chem. Eng. 10, 107283 https://doi.org/10.1016/j.jece.2022.10728.
Liou, T.H., Wang, S.Y., Lin, Y.T., Yang, S., 2022b. Sustainable utilization of rice husk waste for preparation of ordered nanostructured mesoporous silica and mesoporous carbon: Characterization and adsorption performance. Colloid Surf. A-Physicochem. Eng. Asp. 63, 128150 https://doi.org/10.1016/j.colsurfa.2021.128150.
Liou, T.H., Tseng, Y.K., Zhang, T.Y., Liu, Z.S., Chen, J.Y., 2023. Rice husk char as a sustainable material for the preparation of graphene oxide-supported biocarbons with mesoporous structure: A characterization and adsorption study. Fuel 344, 128042. https://doi.org/10.1016/j.fuel.2023.128042.
Liou, T.H., Wu, S.J., 2010. Kinetics study and characteristics of silica nanoparticles produced from biomass-based material. Ind. Eng. Chem. Res. 49 (18), 8379–8387. https://doi.org/10.1021/ie100050t.
Liou, T.H., Yang, C.C., 2011. Synthesis and surface characteristics of nanosilica produced from alkali-extracted rice husk ash. Mater. Sci. Eng. B-Adv. Funct. Solid-State Mater. 176 (7), 521–529. https://doi.org/10.1016/j.mseb.2011.01.007.
Liu, P., Qiu, Z., Shi, H., Song, Y., Zhao, D., Wang, P., Wang, T., Bao, X., 2023a. Reducing the diffusion barriers of Pt/Beta catalyzed n-hexane isomerization by SBA-15 addition and high-energy milling. Microporous Mesoporous Mat. 356, 112591 https://doi.org/10.1016/j.micromeso.2023.112591.
Liu, C., Wei, Q., Zhou, Y., Liu, X., Deng, K., Huang, W., Liu, H., Yu, Z., 2023b. A study on the role of Ti/Si atomic ratios in the hydrodenitrogenation activity of NiMo/TiO2-SiO2 catalyst. Fuel 338, 126922. https://doi.org/10.1016/j.fuel.2022.126922.
Liu, Z., Zhang, Z., Zhou, Y., Wang, Z., Du, M., Wen, Z., Yan, B., Ma, Q., Liu, N., Xue, B., 2024. Phosphotungstic acid supported on Zr-SBA-15 as an efficient catalyst for one-pot conversion of furfural to γ-valerolactone. Fuel 356, 129631. https://doi.org/10.1016/j.fuel.2023.129631.
Luo, F., Li, M., Liang, X., Yang, J., Wang, S., Gao, X., Zhang, Z., Fang, Y., 2023. Self-assembled TiO2/MOF on corrugated paper as a recyclable and efficient composite for dual-channel dye removal. J. Clean Prod. 422, 138679 https://doi.org/10.1016/j.jclepro.2023.138679.
Ma, W., Wang, Y., Huang, L., Yan, L., Kasal, B., 2023. Natural and recycled aggregate concrete containing rice husk ash as replacement of cement: mechanical properties, microstructure, strength model and statistical analysis. J. Build. Eng. 66, 105917 https://doi.org/10.1016/j.jobe.2023.105917.
Mosaberpanah, M.A., Umar, S.A., 2020. Utilizing rice husk ash as supplement to cementitious materials on performance of ultra high performance concrete: – A review. Mater. Today Sustain. 7–8, 100030 https://doi.org/10.1016/j.mtsust.2019.100030.
Parnicka, P., Lisowski, W., Klimczuk, T., Mikolajczyk, A., Zaleska-Medynska, A., 2022. A novel (Ti/Ce)UiO-X MOFs@TiO2 heterojunction for enhanced photocatalytic performance: Boosting via Ce4+/Ce3+ and Ti4+/Ti3+ redox mediators. Appl. Catal. B-Environ. 310, 121349 https://doi.org/10.1016/j.apcatb.2022.121349.
Paulista, L.O., Ferreira, A.F.P., Castanheira, B., Đolic, M.B., Martins, R.J.E., Boaventura, R.A.R., Vilar, V.J.P., Silva, T.F.C.V., 2024. Solar-driven thermo-photocatalytic CO2 methanation over a structured RuO2:TiO2/SBA-15 nanocomposite at low temperature. Appl. Catal. B-Environ. 340, 123232 https://doi.org/10.1016/j.apcatb.2023.123232.
Prasara-A, J., Gheewala, S.H., 2017. Sustainable utilization of rice husk ash from power plants: A review. J. Clean Prod. 167, 1020–1028. https://doi.org/10.1016/j.jclepro.2016.11.042.
Qamar, O.A., Jamil, F., Inayat, A., Akhter, P., Hussain, M., 2024. Upgrading catalytic properties of green synthesized TiO2 for green fuel production from apricot seeds oil. Fuel 355, 129516. https://doi.org/10.1016/j.fuel.2023.129516.
Qin, X., Ji, Y., Nong, L., Wang, C., Li, H., Xie, C., Ji, L., Zhu, A., 2023. Oxygen vacancy-rich C/Ti3C2/(001)TiO2 hollow microspheres and the photocatalytic degradation of organic pollutants. Colloid Surf. A-Physicochem. Eng. Asp. 666, 131258 https://doi.org/10.1016/j.colsurfa.2023.131258.
Raja, K., Venkatachalam, S., Vishnuvardhan, K., Krishnan, R.S.R., Selvan, V.T., Vetriselvan, N., 2022. A review on soil stabilization using rice husk ash and lime sludge. Mater. Today: Proc. 65, 1205–1212. https://doi.org/10.1016/j.matpr.2022.04.178.
Rajendran, S., Blanco, A., Gnanasekaran, L., Jalil, A.A., Chen, W.H., Gracia, F., 2023. Harvesting visible light for enhanced catalytic degradation of wastewater using TiO2@Fe3O4 embedded on two dimensional reduced graphene oxide nanosheets. Chemosphere 345, 140418. https://doi.org/10.1016/j.chemosphere.2023.140418.
Sales, G.S., França, A.A.C,. Cruz-Filho, J.F., Moraes, C.A.F., Neto, A.R.S., Sales, A.G.C., Santos, R.S., Jr, G.E.L., 2023. Photodegradation mechanism of metronidazole on nanostructured material type SBA-15/TiO2, J. Environ. Chem. Eng. 11, 110335. doi: 10.1016/j.jece.2023.1103355.
Sharma, M.V.P., Kumari, V.D., 2008. M. Subrahmanyam, TiO2 supported over SBA-15: An efficient photocatalyst for the pesticide degradation using solar light. Chemosphere 73, 1562–1569. https://doi.org/10.1016/j.chemosphere.2008.07.081.
Signoretto, M., Ghedini, E., Trevisan, V., Bianchi, C.L., Ongaro, M., Cruciani, G., 2010. TiO2–MCM-41 for the photocatalytic abatement of NOx in gas phase. Appl. Catal. B-Environ. 95, 130–136. https://doi.org/10.1016/j.apcatb.2009.12.019.
Srinithi, S., Balakumar, V., Chen, T.W., Chen, S.M., Akilarasan, M., Lou, B.S., Yu, J., 2023. In-situ fabrication of TiO_2-MWCNT composite for an efficient electron transfer photocatalytic rhodamine B dye degradation under UV–visible light. Diam. Relat. Mat. 138, 110245 https://doi.org/10.1016/j.diamond.2023.110245.
Subramani, K., Shunmugasundaram, S., Duraisamy, V., Ilavarasi, R., Kumar, S.M.S., Sathish, M., 2022. Dual heteroatoms doped SBA-15 templated porous carbon for symmetric supercapacitor in dual redox additive electrolyte. J. Colloid Interface Sci. 606, 286–297. https://doi.org/10.1016/j.jcis.2021.08.002.
Sultana, R., Liba, S.I., Rahman, M.A., Yeachin, N., Syed, I.M., Bhuiyan, M.A., 2023. Enhanced photocatalytic activity in RhB dye degradation by Mn and B co-doped mixed phase TiO2 photocatalyst under visible light irradiation. Surf. Interfaces 42, 103302. https://doi.org/10.1016/j.surfin.2023.103302.
Tan, M., Zhang, W., Liu, H., Zhang, J., Guo, Z., Ma, Q., Xu, Q., Hooshyari, K., Su, H., 2024. Revolutionizing high-temperature polymer electrolyte membrane fuel cells: Unleashing superior performance with vertically aligned TiO2 nanorods supporting ordered catalyst layer featuring Pt nanowires. Fuel 357, 130084. https://doi.org/10.1016/j.fuel.2023.130084.
Teixeira, R.A., Lima, E.C., Benetti, A.D., Thue, P.S., Cunha, M.R., Cimirro, N.F.G.M., Sher, F., Dehghani, M.H., dos Reis, G.S., Dotto, G.L., 2021. Preparation of hybrids of wood sawdust with 3-aminopropyltriethoxysilane. application as an adsorbent to remove Reactive Blue 4 dye from wastewater effluents. J. Taiwan Ins Chem. Eng. 125, 141152 https://doi.org/10.1016/j.jtice.2021.06.007.
Ulagesan, S., Santhamoorthy, M., Phan, T.T.V., Alagumalai, K., Thirupathi, K., Kim, S.C., Nam, T.J., Choi, Y.H., 2022. Mesoporous silica (SBA-15) with enriched amidoxime functionalities for pH-controlled anticancer drug delivery. Inorg. Chemi. Commun. 146, 110132 https://doi.org/10.1016/j.inoche.2022.110132.
Urbanek, K., Jakiminska, A., Spilarewicz, K., Macyk, W., 2023. Defective cobalt and copper tungstates mixtures with TiO2 for photocatalytic CO2 reduction. Appl. Surf. Sci. Adv. 18, 100473 https://doi.org/10.1016/j.apsadv.2023.100473.
Wang, Y., Bai, X., 2023. Efficient catalytic hydrogen storage of N-ethylcarbazole over RuNi alloy nanoparticles loaded on SBA-15 prepared by electrostatic adsorption. Fuel 331, 125709. https://doi.org/10.1016/j.fuel.2022.125709.
Wei, P., Zhang, Y., Huang, Y., Chen, L., 2023. Structural design of SiO2/TiO2 materials and their adsorptionphotocatalytic activities and mechanism of treating cyanide wastewater. J. Mol. Liq. 377, 121519 https://doi.org/10.1016/j.molliq.2023.121519.

Xu, Z., Xu, D., Li, S., Liu, Z., Gao, X., Cheng, L., Liu, Y., 2023. J. Sun, Preparation, sustained-release and antibacterial activity of SBA-15/CG antibacterial agent. Mater. Lett. 344, 134432 https://doi.org/10.1016/j.matlet.2023.134432.

Yang, J., Zhang, J., Zhu, L., Chen, S., Zhang, Y., Tang, Y., Zhu, Y., Li, Y., 2006. Synthesis of nano titania particles embedded in mesoporous SBA-15: Characterization and photocatalytic activity. J. Hazard. Mater. B137, 952–958. https://doi.org/10.1016/j.jhazmat.2006.03.017.

Yoganandhan, N., Tamizhdurai, P., Kavitha, C., Mangesh, V.L., Kumar, N.S., Al-Fatesh, A. S., Kumaran, R., Basivi, P.K., 2023. TiO2/SO4/Ni@SBA-15 catalysts for the selective oxidation of veratryl alcohol to veratraldehyde in a continuous reactor. Mol. Catal. 546, 113250 https://doi.org/10.1016/j.mcat.2023.113250.

Yuan, M., Zhong, S., Li, G., Fan, G., Yu, X., 2024. Architecture of urchin-like TiO2 integrated ultrasmall Rh nanoparticles with oxygen vacancy-reinforced electronic metal-support interaction for boosting hydrogen production from ammonia borane hydrolysis. Fuel 358, 130200. https://doi.org/10.1016/j.fuel.2023.130200.

Zhang, T.Y., Liou, T.H., Chiu, S.E., Hsu, C.C., Liu, W.Y., 2023. A sustainable route for production of graphene oxide-contained nanostructured carbons from rice husk waste and its application in wastewater treatment. Environ. Technol. Innov. 32, 103270 https://doi.org/10.1016/j.eti.2023.103270.

Ziarani, G.M., Moradi, R., Mohajer, F., Badiei, A., 2022. 2-Chloroquinoline-3-carbaldehyde modified nanoporous SBA-15-propylamine (SBA-Pr-NCQ) as a selective and sensitive Ag+ ion sensor in aqueous media. J. Phys. Chem. Solids 161, 110399. https://doi.org/10.1016/j.jpcs.2021.110399.